Surface-directed and bulk spinodal decomposition compete to decide the morphology of bimetallic nanoparticles

P. Pankaj, Saswata Bhattacharyya*, and Subhradeep Chatterjee*
Department of Materials Science and Metallurgical Engineering,
Indian Institute of Technology, Hyderabad, 502284, Telangana, India
(*saswata@msme.iith.ac.in, subhradeep@msme.iith.ac.in)
(Dated: July 8, 2022)

An embedded-domain phase-field formalism is used for studying phase transformation pathways in bimetallic nanoparticles (BNPs). Competition of bulk and surface-directed spinodal decomposition processes and their interplay with capillarity are identified as the main determinants of BNP morphology. The former is characterized by an effective bulk driving force $\Delta\tilde{f}$ which increases with decreasing temperature, while the latter manifests itself through a balance of interfacial energies captured by the contact angle θ. The simulated morphologies, namely, core-shell, Janus and inverse core-shell, cluster into distinct regions of the $\Delta\tilde{f}$-θ space. Variation of θ with $\Delta\tilde{f}$ in the Ag-Cu alloy system is computed as a function of temperature using a CALPHAD approach in which surface energies are estimated from a modified Butler equation. This $\theta-\Delta\tilde{f}$ trajectory for Ag-Cu, when superimposed on the morphology map, enables the prediction of different morphological transitions as a function of temperature. Therefore, the study establishes a unique thermodynamic framework coupled with phase-field simulations for predicting and tailoring nanoparticle morphology through a variation of processing temperature.

INTRODUCTION

Properties of bimetallic nanoparticles (BNPs) used in diverse fields such as catalysis, photonics, spintronics and biomedical-sensing [1–3] depend crucially on their morphology. Core-shell (CS) and Janus are the most commonly reported morphologies: CS morphology consists of an outer shell of the lower surface energy component surrounding a core of the other component, while Janus is characterized by the two components forming two opposite faces of a particle with their common interface extending to the surface. An inverse core-shell (ICS) morphology, where the higher surface energy component forms the shell, has also been observed in a few cases [4, 5].

A fundamental understanding of morphological development in BNPs is crucial for tailoring their properties. First principles [6] and atomistic [7] simulations, as well as classical thermodynamics [8] have been employed to find the lowest energy morphology of BNPs. However, these approaches generally do not address kinetic aspects of morphological development. Since many commonly used BNP systems like Ag-Cu, Ag-Ni, Au-Co, Co-Cu, etc. exhibit solid-state immiscibility, spinodal decomposition (SD) presents a likely kinetic pathway for morphology development in BNPs [9].

Phase-field models have been employed very successfully for studying microstructure development in bulk immiscible systems systems using the Fourier spectral method [10]. For finite systems with complex geometries, embedding the system of interest in a larger computational domain has proven to be an effective strategy for dealing with the non-periodicity of the domain of interest [11–14]. In addition to Dirichlet, Neumann and Robin boundary conditions, Yu et al. developed a methodology [13] to impose a contact angle boundary condition for studying phase transformations in contact with an external surface. However, if one wishes to capture the *in situ* development of three-phase contacts (or their absence) on the surface, a different approach involving a modification of the system's free energy can be adopted.

Recently, we presented such an embedded-domain phase-field model (EPFM) [15] using which correct contact angles could be naturally recovered without imposing them directly through boundary conditions. This model was was used to understand how contact angle and particle size influenced the morphology development in BNPs. However, the role of temperature, which is an important parameter from a processing perspective, on BNP morphology was not addressed. Temperature, or equivalently, undercooling below a critical temperature, can exert a strong influence on the phase separation process by altering the driving force for bulk SD. In addition, in confined systems such as BNPs, surface directed SD (SDSD) presents another mode of microstructural evolution which may also be influenced by temperature through its effect on surface and interfacial energies. Interplay between these two alternative mechanisms and their interactions with capillarity give rise to different BNP morphologies. In this paper, we use EPFM to systematically investigate this process, and by carrying out further thermodynamic computations, identify the relevant physical parameter groups that can be used to understand and predict morphology selection in BNPs as a function of temperature.

MODEL FORMULATION

In the EPFM formalism [15] illustrated schematically in Fig. 1, a BNP system consisting of atomic species A and B is modeled by placing an isolated particle (β) in an inert matrix (α). A scaled composition field c describes phase separation of an initially homogeneous β to a mixture of β_1 and β_2 phases with equilibrium compositions $c^e_{\beta_1}$ and $c^e_{\beta_2}$, respectively. We use $c=(X-X^e_{\beta_1})/(X^e_{\beta_2}-X^e_{\beta_1})$ for the scaling where X denotes the mole fraction of B and X_{β_i} is the equilibrium composition of phase β_i at a given temperature. An auxiliary non-conserved phase-field variable ϕ is used to distinguish

the particle from the matrix; we use a stationary and radially symmetric tanh profile for ϕ that varies smoothly across the particle surface from 0 in the matrix side to 1 inside the particle [15]. Total free energy of the system is then expressed as:

$$\mathscr{F} = \frac{1}{V_m}\int_\Gamma \Big(f(c,\phi) + \kappa_\phi |\nabla\phi|^2 + \kappa_c |\nabla c|^2 \Big) d\Gamma, \qquad (1)$$

where V_m is the molar volume, f is bulk free energy density, κ_c and κ_ϕ are gradient energy coefficients associated with c and ϕ, respectively, and Γ is the volume of the whole computational domain.

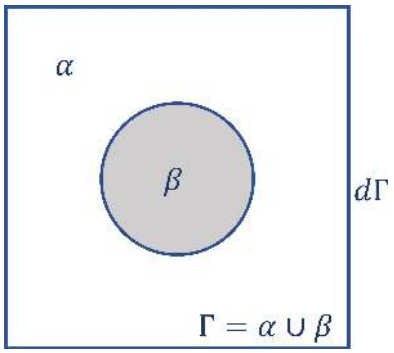

FIG. 1: Computational domain Γ consisting of an isolated nanoparticle β (physical domain of interest) in an inert matrix α. Periodic boundary conditions are imposed on the domain boundary $d\Gamma$.

Defining an interpolating function $h(\phi) = \phi^3(10 - 15\phi + 6\phi^2)$ that connects α and β (with ϕ being 0 and 1 inside α and β, respectively), the bulk free energy density f is given as $f(c,\phi) = h(\phi)f^\beta + (1-h(\phi))f^\alpha + \omega(c)g(\phi)$. Here $\omega(c)g(\phi) = \omega_0(1-\chi c)\phi^2(1-\phi)^2$ describes the free energy barrier between α and β, ω_0 sets the barrier height and χ controls solute segregation at the particle-matrix interface [15]. We use the following forms of free energy for α and β:

$$\begin{aligned} f^\alpha &= f_0^m (c - c_\alpha^e)^2, \\ f^\beta &= f_0^p (c - c_{\beta_1}^e)^2 (c - c_{\beta_2}^e)^2. \end{aligned} \qquad (2)$$

The scaled equilibrium compositions $c_\alpha^e, c_{\beta_1}^e, c_{\beta_2}^e$ are chosen to be 0.5, 0 and 1, respectively, and f_0^p and f_0^m are temperature-dependent constants. Evolution of composition field within the particle is described by the Cahn-Hilliard equation:

$$\frac{\partial c}{\partial t} = \nabla \cdot M(\phi) \nabla \frac{\delta \mathscr{F}}{\delta c}. \qquad (3)$$

We constrain the matrix to remain inert with respect to solute diffusion by choosing $M(\phi) = M_c h(\phi)$, with M_c being the effective atomic mobility of solute in the particle. Eq. (3) is solved numerically using a semi-implicit Fourier spectral method [16–18]. We non-dimensionalize all parameters in the equations using characteristic length L_c, time τ_c and energy E_c. Details of the non-dimensionalization procedure are provided Supplementary Information A; further details of the model and its numerical implementation can be found elsewhere [15].

Energies of α-β_1, α-β_2 and β_1-β_2 interfaces, designated as σ_1, σ_2 and σ_{12}, are obtained from the equilibrium composition profiles $c^e(x)$ across the respective interfaces:

$$\begin{aligned} \sigma = \frac{1}{V_m}\int \Big[& f(c^e(x),\phi(x)) + \kappa_\phi |\nabla\phi|^2 + \kappa_c |\nabla c^e(x)|^2 \\ & - \Big\{ (1-c^e(x))\mu_A^e + c^e(x)\mu_B^e \Big\} \Big] dx, \end{aligned} \qquad (4)$$

where μ_i^e $(i = A, B)$ denotes the equilibrium chemical potential of component i in any one the coexisting phases across the interface.

The surface and interfacial energies define the contact angle θ at the triple junction between the phases as:

$$\cos\theta = \frac{\sigma_1 - \sigma_2}{\sigma_{12}}. \qquad (5)$$

Phase transformations within the particle need not always yield triple junctions at the surface. Cahn, in his classic paper on "Critical Point Wetting", described a condition that precluded the formation of a triple junction. He defined this *spontaneous* wetting condition to be $\sigma_1 - \sigma_2 \geq \sigma_{12}$; the equality condition corresponds to $\theta = 0°$, while θ become undefined for the inequality condition. In the latter case, the phase with the low surface energy develops a continuous layer on the surface.

Non-zero χ leads to preferential solute segregation to one of the surfaces by creating imbalance between the 'surface' energies σ_1 and σ_2 – its key role on BNP morphology has already been explored in detail [15]. Here, we keep χ and particle size fixed, and investigate the competition of bulk SD and SDSD in deciding the BNP morphology (CS, ICS and Janus) by varying f_0^p, ω_0 and κ_c. Note that these variable also control θ. Since each of these parameter combinations gives rise to one of these three morphologies, we performed simulations over a large set of parameters and classified the results in terms of driving force and contact angle.

RESULTS AND DISCUSSION

A. Simulation of BNP morphologies

All simulations begin with an initially homogeneous, axisymmetric β particle with composition $c = 0.5$ quenched inside the miscibility gap. A small initial noise ($\pm 1\%$) mimicking thermal fluctuations is applied to trigger bulk SD. Figs. 2 and 3 present time snapshots of evolution of stable and metastable morphologies corresponding to representative parameter sets listed in Table I. In these figures, green color represents the solute-poor β_1 phase, blue the solute-rich β_2 phase, and grey the undecomposed β with $c = 0.5$.

In all cases, SDSD precedes bulk-SD and forms alternate solute-rich and solute-lean rings which grow inward. When bulk SD starts in the interior of the particle, it creates intertwined compositionally modulated domains that interact with

TABLE I: Variation of surface and interfacial energies and contact angle θ with model parameters. Figure numbers refer to snapshots of morphological evolution for the corresponding set of parameters.

Set	f_0^p	κ_c	ω_0	σ_1	σ_2	σ_{12}	θ	Figure no.
1	8	1	12	4.19	3.09	0.94	wetting	2a-2e
2	6	2	3.75	1.77	1.44	1.15	74°	2f-2j
3	4	1	6	2.21	1.76	0.67	48°	3a-3e
4	2	8	6	2.24	1.86	1.33	73.5°	3f-3j
5	4	2	5	1.98	1.60	0.94	66°	3k-3o

the rings growing from the surface to the center. Depending on the chosen parameter set, domain coarsening proceeds along different pathways to produce the final BNP configuration. A Janus structure is formed when coarsening disrupts the continuity of ring-like structures at the surface, and CS or ICS results otherwise.

Figs. 2(a-e) is an example of a typical evolution pattern leading to a stable CS morphology (set 1 of Table 1). It occurs irrespective of the driving force if the spontaneous wetting condition is satisfied (*i.e.*, $\sigma_1 - \sigma_2 \geq \sigma_{12}$). For large θ, if bulk driving force is sufficiently high to break the outermost layer, we obtain stable Janus morphology. A typical sequence of its formation is presented in Figs. 2(f-j) which corresponds to parameter set 2 of Table I.

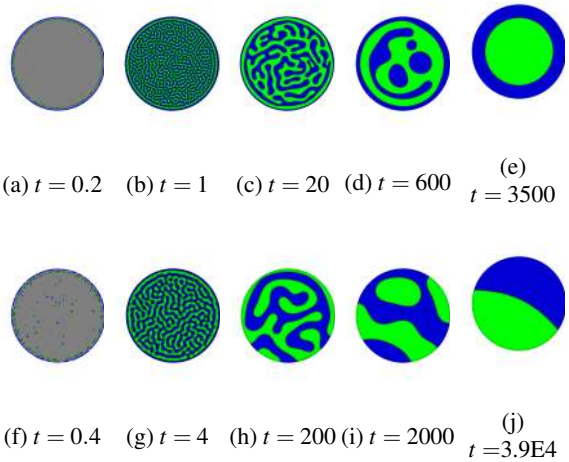

(a) $t = 0.2$ (b) $t = 1$ (c) $t = 20$ (d) $t = 600$ (e) $t = 3500$

(f) $t = 0.4$ (g) $t = 4$ (h) $t = 200$ (i) $t = 2000$ (j) t =3.9E4

FIG. 2: Time snapshots of morphological evolution of stable CS (top row) and Janus (bottom row) configurations. Non-dimensional times are indicated below each snapshot.

Parameter sets 3-5 of Table 1 correspond to intermediate values of driving force (which scales with f_0^p) and θ which result in metastable configurations shown in Figure 3. For example, Figs. 3(a-e) shows how a CS morphology can develop for small non-zero θ's if the driving force for bulk spinodal is also small. Thus, the spontaneous wetting condition is only a sufficient condition – stable CS forms when it is satisfied, but a metastable CS can develop even when it is not.

On the other hand, one obtains a metastable ICS morphology when the driving force is small but θ is large, as demonstrated by the typical evolution patterns in Figs. 3(f-j) and Figs. 3(k-o). When surface effects dominate over the bulk, an onion-like ring structure develops initially (Figs. 3a-3b), which coarsens subsequently (Figs. 3(a-e)) to form a metastable ICS morphology. It is also possible that we get metastable ICS/CS even in the presence of bulk spinodal. As shown in Figs. 3(f-o), the bulk driving force in this case is not sufficiently high enough to achieve a stable Janus configuration, and domain coarsening leads to an ICS configuration. Between the two evolutionary paths to ICS, the latter is observed when the driving force is higher.

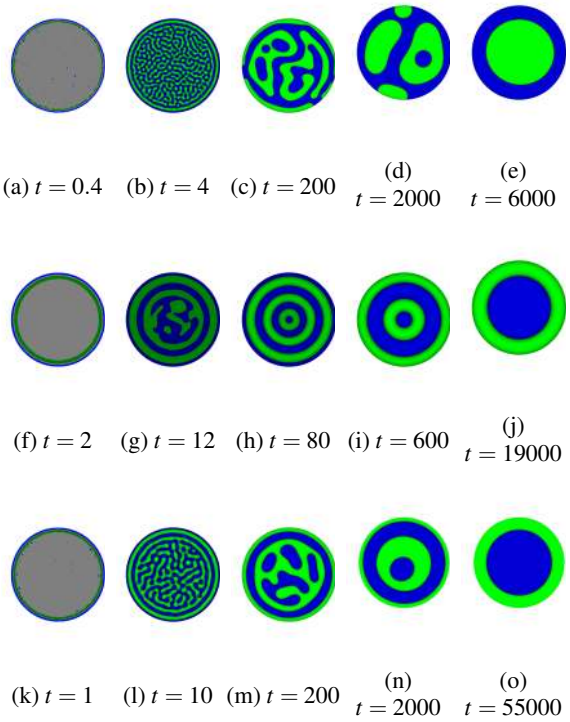

(a) $t = 0.4$ (b) $t = 4$ (c) $t = 200$ (d) $t = 2000$ (e) $t = 6000$

(f) $t = 2$ (g) $t = 12$ (h) $t = 80$ (i) $t = 600$ (j) $t = 19000$

(k) $t = 1$ (l) $t = 10$ (m) $t = 200$ (n) $t = 2000$ (o) $t = 55000$

FIG. 3: Time snapshots of metastable CS (top row) and ICS (middle and bottom rows) evolution. Non-dimensional times are indicated below for each snapshot.

As shown in Fig. 4, however, the CS at non-zero θ and ICS configurations are metastable, as they relax to more stable structures when subjected to a sustained white noise [19]. Here the initial configurations for the simulations are the final metastable ones shown in Fig. 3. With increasing time, the concentric structures break down and evolve to form Janus. The time taken for the metastable-to-stable morphological transition is very large because the difference of the energies between the metastable (CS/ICS) and stable (Janus) configuration is very small, resulting in very sluggish diffusion. Therefore, these can be termed as kinetically trapped configurations [15, 20, 21].

To understand the formation of different morphologies as a function of the model parameter sets, one needs to relate the competing processes of bulk SD and SDSD. For bulk SD, f_0^p

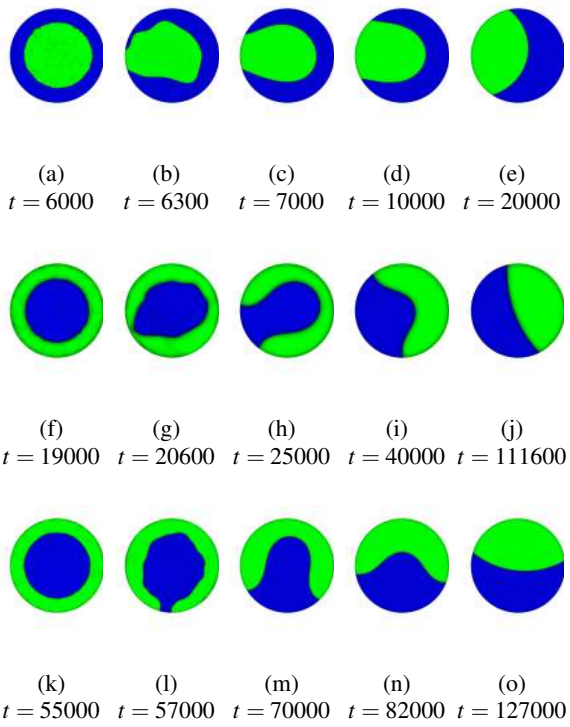

FIG. 4: Time snapshots of transition from metastable CS/ICS to stable CS configurations brought about by sustained noise. Non-dimensional times are indicated below for each snapshot.

sets the driving force Δf, defined as the difference between the free energy of non-equilibrium initial β state and that of the final state made up of equal parts of equilibrium β_1 and β_2 phases:

$$\Delta f = f^{\beta}(c=0.5) - \frac{1}{2}\left[f^{\beta}(c=c^{e}_{\beta_1}) + f^{\beta}(c=c^{e}_{\beta_2})\right] = f_0^{p}/16 \text{ (using Eq. (2))}. \quad (6)$$

Δf, together with κ_c, also determines the interfacial energy σ_{12} of the system as [22]:

$$\sigma_{12} = \frac{1}{3V_m}\left[c^{e}_{\beta_2}(T) - c^{e}_{\beta_1}(T)\right]^3 \sqrt{\kappa_c \Delta f(T)}. \quad (7)$$

Both Δf and σ_{12} increase with decreasing T (or increasing undercooling ΔT).

The surface energies σ_1 and σ_2, and their difference $\Delta\sigma$, on the other hand, scale with the height of the free energy barrier ω_0. While Δf controls bulk SD within the particle, ω_0 influences SDSD by defining $\Delta\sigma$ – the larger the $\Delta\sigma$, the easier it is to initiate SDSD. We now define a normalized driving force for bulk phase separation, $\Delta\tilde{f}$, by taking the ratio of Δf to $\Delta\sigma$.

Fig. 5 presents the essence of all simulations by assigning the location of BNP configuration in the space of model parameters $\Delta\tilde{f}$ and θ. The map clearly demarcates three distinct regions in this space: high $\Delta\tilde{f}$-high θ for Janus, low $\Delta\tilde{f}$-high θ for ICS, and the intervening region for CS. The region of high $\Delta\tilde{f}$-low θ is physically inaccessible since high $\Delta\tilde{f}$ implies either high Δf or low ω_0, which increases σ_{12} or decreases $\Delta\sigma$, respectively, and thereby lead to high θ.

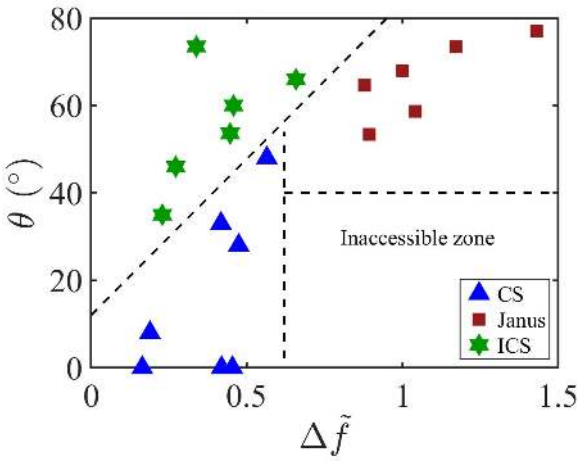

(a)

FIG. 5: Simulated stable and metastable BNP configurations in the $\Delta\tilde{f}$–θ space. Dashed lines are drawn to delineate regions of where Janus, CS and ICS morphologies are observed.

When the spontaneous wetting condition is satisfied ($\theta = 0°$ or undefined), CS is the final configuration irrespective of $\Delta\tilde{f}$. Also, for a given θ, a metastable CS configuration is preferred over ICS at larger $\Delta\tilde{f}$. At lower $\Delta\tilde{f}$, SDSD creates alternate concentric rings extending towards the center, with segregation giving rise to an outermost β_1 ring [15]. Subsequently, ring-coarsening leads to the ICS structure. In contrast, bulk SD dominates at higher $\Delta\tilde{f}$, resulting in interactions between inner interconnected domains and the outermost β_1 ring during coarsening. Subsequently, the latter is replaced by β_2, leading to metastable CS. Note that these interactions do not yield the stable Janus configuration, because, in this case, $\Delta\sigma$ remains sufficiently large to cause β_2 to preferentially spread along the surface and β_1 to recede.

B. Computation of chemical and capillary forces for Ag-Cu

Fig. 5 demonstrated how different morphologies clustered around in distinct regions of the driving force – contact angle space. This space essentially represents the interplay of chemical and capillary forces, and temperature is one of the key physical parameters that directly or indirectly controls them. The chemical driving force for phase separation, Δf, for a given system can be obtained as a function of temperature in a relatively straightforward way from its CALPAHD data. Capillarity, on the other hand, is manifested through the contact angle θ, which itself is defined in terms of interfacial and surface energies ($\sigma_1, \sigma_2, \sigma_{12}$). Reliable values of the latter as a function of temperature are often difficult to measure

experimentally. Nevertheless, here we attempt to arrive at fair estimates of these energies using the available data and thermodynamic correlations. We consider the Ag-Cu system as an example and proceed to compute the temperature dependence of these quantities.

1. *Driving force for phase separation*

The molar bulk free energy F_m of the Cu-Ag solid solution can be expressed through a Redlich-Kister polynomial as:

$$F_m = \left[X_{\rm Ag}F^0_{\rm Ag} + X_{\rm Cu}F^0_{\rm Cu}\right] + RT\left[X_{\rm Cu}\ln X_{\rm Cu} + X_{\rm Ag}\ln X_{\rm Ag}\right] + X_{\rm Cu}X_{\rm Ag}\left[L_0 + L_1(X_{\rm Ag} - X_{\rm Cu})\right] \quad (8)$$

where X_i's ($i =$ Cu, Ag) are the mole fractions component i in the solution. The first bracketed group in the right hand side is the mixture free energy contribution with F^0_i's being the standard free energies of the pure components which can be found in the SGTE database [23]. The second group is the contribution from the ideal solution part of free energy ($F_m^{\rm id,bulk}$) and the last term represents the excess contribution ($F_m^{\rm ex,bulk}$). The temperature-dependent interaction parameters for the Cu-Ag solid solution are given as $L_0 = 34532 - 9.178T$ and $L_1 = -5996 + 1.725T$ [24].

Equilibrium solute mole fractions X^e_i in Cu-rich and Ag-rich solid solutions below the critical temperature T_c are computed using the conditions for chemical equilibrium:

$$\mu^{\rm Cu_{ss}}_{\rm Ag} = \mu^{\rm Ag_{ss}}_{\rm Ag}, \quad \mu^{\rm Cu_{ss}}_{\rm Cu} = \mu^{\rm Ag_{ss}}_{\rm Cu}, \quad (9)$$

where the chemical potentials $\mu_i\,(i = {\rm Cu, Ag})$ evaluated at equilibrium bulk compositions X^e_i are given by

$$\mu_{\rm Cu} = F_m - X_{\rm Ag}\frac{\partial F_m}{\partial X_{\rm Ag}}; \quad \mu_{Ag} = F_m + (1 - X_{\rm Ag})\frac{\partial F_m}{\partial X_{\rm Ag}}. \quad (10)$$

The free energy of mixing for an alloy composition $X_{\rm Ag}$ is expressed as

$$\Delta F_{\rm mix} = F_m - (X_{\rm Cu}\mu^e_{\rm Cu} + X_{\rm Ag}\mu^e_{\rm Ag}). \quad (11)$$

The driving force for bulk spinodal, Δf, is the maximum value of $\Delta F_{\rm mix}$ over the entire composition range (*i.e.*, maximum of the $\Delta F_{\rm mix} - X$ curve). It is evaluated and plotted in Fig. 6a for the temperature range of 400-800 K. The plot shows that Δf decreases monotonically with increasing temperature. Using the same thermodynamic data, we also compute the equilibrium mole fractions X^e_i ($i =$ Cu, Ag) in both Cu- and Ag-rich solutions which are required for estimating the interfacial energy.

2. *Interfacial energy*

The temperature dependence of the interfacial energy between the Cu- and Ag-rich solid solutions ($\sigma_{\rm Cu-Ag}$) can be computed using Eq. (7). To be able to do so, however, one requires the value of κ_c. We utilize the value of $\sigma_{\rm Cu-Ag} = 0.197$ Jm^{-2} at 800 K obtained from molecular dynamics simulations [7], along with the values of Δf and X^e_i at this temperature calculated in the previous step, and a constant molar volume of 10^{-5} m^{3}mol^{-1}, to compute $\kappa_c = 1.94 \times 10^{-14}$ Jm^{2}mol^{-1}. Since κ_c is generally considered to be temperature-independent for a given system, we use this constant value in Eq. (7) to compute $\sigma_{\rm Cu-Ag}$ in the temperature range of 400-1200 K.

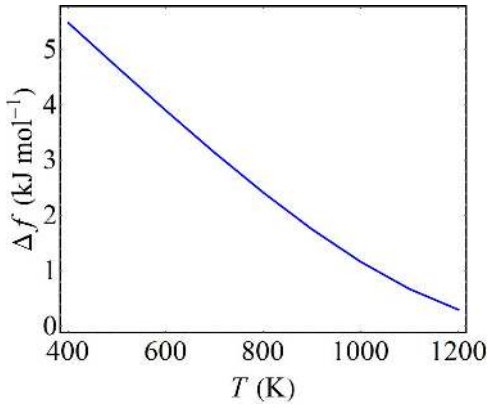

(a)

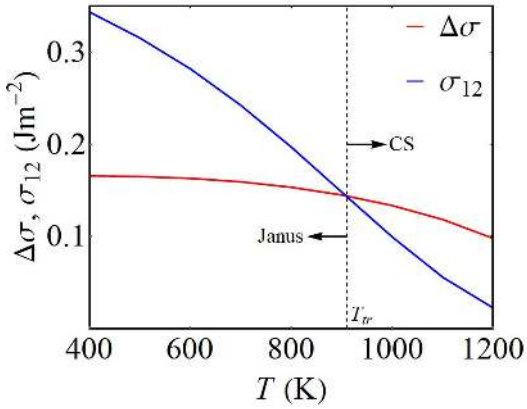

(b)

FIG. 6: (a) Variation of Δf with temperature for the Ag-Cu system computed using its CALPHAD data. (b) Temperature-dependence of interfacial and surface energies of Cu-poor and Cu-rich solid solution phases. Temperature of transition (T_{tr}) from stable CS to Janus morphology is indicated.

3. *Surface energies*

We calculate surface energies $\sigma_{i,\rm ss}$ of the Cu-rich and Ag-rich solid solutions as a function of temperature T using a

modified Butler model [25]:

$$\sigma(T) = \sigma_i^0 + \frac{RT}{A_i}\log\left[\frac{X_i^{\text{surf}}}{X_i^e}\right] + \frac{1}{A_i}[F_i^{\text{ex,surf}}(T, X_i^{\text{surf}}) - F_i^{\text{ex,bulk}}(T, X_i^e)]. \quad (12)$$

Here, $i =$ A, B denote the components Cu and Ag, respectively, σ_i^0 are the surface energies of the pure components, A_i are the molar surface areas, X_i^{surf} are the surface compositions at T, $F_i^{\text{ex,surf}}$ and $F_i^{\text{ex,bulk}}$ are the excess partial molar free energies of i associated with surface and bulk, respectively.

Surface energies of the pure components Eq. (12) are obtained from the correlation

$$\sigma_i^0 = 1.25\sigma_i^{\text{liq}} + \frac{d\sigma}{dT}(T - T_m^i) \quad (13)$$

where σ_i^{liq} is the surface tension of liquid component at its melting point T_m^i and the temperature coefficient of surface energy is taken as -10^{-4} Jm^{-2}K. The partial molar excess free energies for bulk, $F_i^{\text{ex,bulk}}$, can be expressed in terms of X_i^e using Eq. (10), with excess free energy $F^{ex,bulk}$ replacing the total molar free energy F_m. Following Tanaka and Hara [25], we take $F_i^{\text{ex,surf}} = \beta_{mix} F_i^{\text{ex,bulk}}$. The parameter β_{mix} is the ratio of coordination number in the surface to that in the bulk; it is taken as 0.75 for face centered cubic solid solutions. Molar surface areas A_i of the pure components are obtained using the relation $A_i = 1.091 N_0^{1/3} V_m^{2/3}$ where N_0 is the Avogadro's number. Eq. (12) constitutes a set of two simultaneous nonlinear algebraic equations which can now be solved numerically to obtain the unknown surface composition X_i^{surf} for both the terminal phases. Plugging its values in Eq. (10), one can compute the surface energies of the Cu- and Ag-rich solution phases.

Fig. 6b plots the difference of the surface energies, $\Delta\sigma = \sigma_{\text{Cu}_{\text{ss}}} - \sigma_{\text{Ag}_{\text{ss}}}$, and the interfacial energy, $\sigma_{\text{Cu-Ag}}$, with temperature. It shows that although the surface energies themselves vary with temperature, their difference is relatively insensitive to it, changing only slightly at higher temperatures. The interfacial energy, on the other hand, depends strongly with temperature, decreasing steeply at higher temperatures. This is expected, as it must vanish at the critical temperature for the miscibility gap. In terms of the spontaneous wetting criterion (Eq. (5)), temperature of intersection of surface and interfacial energy lines, T_{tr} ($\sim$ 910 K) marks the transition from *stable* CS to Janus morphologies.

C. Connecting phase-field results with thermodynamic computations

We proceed further to obtain a correlation between the effective driving force $\Delta\tilde{f}$ and θ, noting that the latter is defined only for $T \leq T_{tr}$. First, the bulk driving force Δf (in J/mol) for phase separation in Ag-Cu is normalized by the product of surface energy difference $\Delta\sigma$ (in J/m^2) and molar surface area (in m^2/mol). Fig. 7a shows the temperature dependence of $\Delta\tilde{f}$ estimated this way, it is very similar to the variation of Δf with T shown in Fig. 6a. Next, the interfacial and surface energies computed earlier are used to determine how contact angle varies as a function of temperature. This is presented in Fig. 7b, which shows that at high temperatures, θ decreases steeply with decrease in temperature, but the rate of this decrease reduces at lower temperatures. Finally, these variations are combined into a single $\Delta\tilde{f}$-θ plot in Fig. 7c. It shows a monotonic increase of θ with $\Delta\tilde{f}$; however, the slope of the curve is steeper at low-$\Delta\tilde{f}$, gradually becoming gentler with increase in $\Delta\tilde{f}$ (*i.e.*, decrease in T). This line is the trajectory that the system follows in the $\Delta\tilde{f}$-θ space as temperature is reduced, and therefore captures its response to a change in the state variable T. This trajectory is now superimposed on the morphology map which is redrawn in Fig. 7d. It predicts the morphological transitions in Ag-Cu for $T < T_{tr}$: both $\Delta\tilde{f}$ and θ increase with decreasing temperature, and the system moves from a metastable CS to metastable ICS configuration, before finally transitioning into the Janus regime. Thus, depending on the processing conditions, all the three configurations can form in Ag-Cu BNPs, as confirmed by the experimentally observed configurations [5, 26].

Since the temperature dependence of bulk chemical and capillary forces are system specific, it should be noted that the trajectory may not always pass through the metastable ICS region of the map for all alloy systems. However, the insights gained from the study remains valid and provide crucial guidelines and understanding for conducting further experiments aimed at tailoring the BNP morphology.

I. CONCLUSIONS

Results of the present study show how different BNP morphologies can emerge from a competition between two alternative and concomitant mechanisms, namely, bulk and surface-directed spinodal decomposition. Their interplay with capillarity sets up the eventual coarsening pathway toward a steady-state configuration. When we express the results in terms of three physical parameters, namely, driving force, difference in surface energies and contact angle, different morphologies automatically cluster into three distinct regions in the $\Delta\tilde{f} - \theta$ space. This identification of relevant physical parameters appears remarkable, as the computed thermodynamic trajectory for Ag-Cu involving the same variables traverses all the three distinct regions revealing the morphological transitions. We note that morphological transitions for a particular alloy system are sensitive to the nature of temperature-dependence of the relevant variables. Therefore, the exact transition points for different alloys systems will be different.

The following specific conclusions can be drawn from the study:

1. Irrespective of the driving force for bulk spinodal, stable CS forms when the spontaneous wetting condition is satisfied ($\theta = 0°$). This happens at $T \geq T_{tr}$.

2. A combination of low driving force and high contact

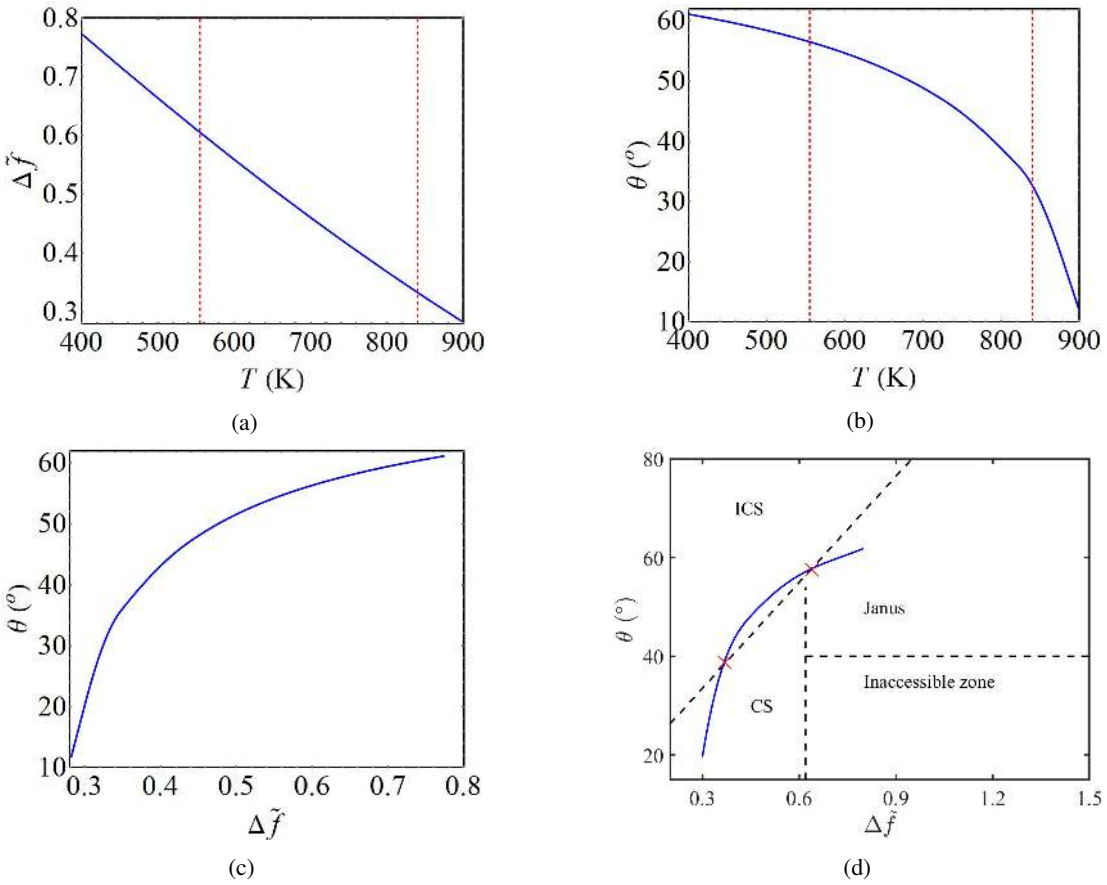

FIG. 7: (a) Temperature-dependence of $\Delta\tilde{f}$. (b) Variation of θ with temperature for the Ag-Cu system computed using its CALPHAD data. (c) Correlation of θ with $\Delta\tilde{f}$. (d) The $\theta - \Delta\tilde{f}$ trajectory for Ag-Cu is superimposed on the morphology map obtained from simulations. CS→ICS and ICS→Janus transitions are indicated by the crosses, and vertical dashed lines are drawn on (a) and (b) to indicate the temperatures for these transitions (the former takes place at the higher T).

angle gives rise to metastable ICS, while metastable CS forms at moderate driving force and lower non-zero θ. Thus, the *spontaneous* wetting condition given by Cahn is found to be a *sufficient*, but not a *necessary* condition for the formation of CS.

3. Janus forms when both bulk driving force and contact angle are large.

4. Trajectory of Ag-Cu in the driving force-contact angle space shows transitions involving CS, ICS and Janus morphologies as a function of temperature.

CONFLICT OF INTEREST

The authors have no conflicts to disclose.

ACKNOWLEDGEMENT

Authors gratefully acknowledge the computational support from DST-NSM Grant DST/NSM/R&D-HPC-Applications/2021/03.

[1] R. Ferrando, *Structure and Properties of Nanoalloys* (Elsevier, 2016).

[2] M. B. Cortie and A. M. McDonagh, Synthesis and optical properties of hybrid and alloy plasmonic nanoparticles, Chemical Reviews **111**, 3713 (2011).

[3] D. Medina-Cruz, B. Saleh, A. Vernet-Crua, A. Nieto-Argüello, D. Lomelí-Marroquín, L. Y. Vélez-Escamilla, J. L. Cholula-Díaz, J. M. García-Martín, and T. Webster, Bimetallic nanoparticles for biomedical applications: A review, in *Racing for the Surface: Antimicrobial and Interface Tissue Engineering*, edited by B. Li, T. F. Moriarty, T. Webster, and M. Xing

(Springer International Publishing, Cham, 2020) pp. 397–434.
[4] M. Tsuji, S. Hikino, R. Tanabe, and D. Yamaguchi, Synthesis of Ag@Cu core–shell nanoparticles in high yield using a polyol method, Chemistry Letters **39**, 334 (2010).
[5] T. Nakamura, Y. Tsukahara, T. Yamauchi, T. Sakata, H. Mori, and Y. Wada, Preparation of Ag core–Cu shell nanoparticles by microwave-assisted alcohol reduction process, Chemistry Letters **36**, 154 (2007).
[6] R. Ferrando, Symmetry breaking and morphological instabilities in core-shell metallic nanoparticles, Journal of Physics Condensed Matter **27**, 13003 (2015).
[7] M. Chandross, Energetics of the formation of Cu–Ag core–shell nanoparticles, Modelling and Simulation in Materials Science and Engineering **22**, 075012 (2014).
[8] C. W. Yuan, S. J. Shin, C. Y. Liao, J. Guzman, P. R. Stone, M. Watanabe, J. W. Ager, E. E. Haller, and D. C. Chrzan, Structure map for embedded binary alloy nanocrystals, Applied Physics Letters **93**, 193114 (2008).
[9] G. Radnóczi, E. Bokányi, Z. Erdélyi, and F. Misják, Size dependent spinodal decomposition in Cu-Ag nanoparticles, Acta Materialia **123**, 82 (2017).
[10] L. Chen and J. Shen, Applications of semi-implicit fourier-spectral method to phase field equations, Computer Physics Communications **108**, 147 (1998).
[11] A. Bueno-Orovio, V. M. Pérez-García, and F. H. Fenton, Spectral methods for partial differential equations in irregular domains: The spectral smoothed boundary method, SIAM Journal on Scientific Computing **28**, 886 (2006).
[12] X. Li, J. Lowengrub, A. R Ratz, and A. Voigt, Solving pdes in complex geometries, Communications in Mathematical Sciences **7**, 81 (2009).
[13] H. C. Yu, H. Y. Chen, and K. Thornton, Extended smoothed boundary method for solving partial differential equations with general boundary conditions on complex boundaries, Modelling and Simulation in Materials Science and Engineering **20**, 075008 (2012).
[14] S. Poulsen and P. Voorhees, Early stage phase separation in ternary alloys: A test of continuum simulations, Acta Materialia **113**, 98 (2016).
[15] P. Pankaj, S. Bhattacharyya, and S. Chatterjee, Competition of core-shell and Janus morphology in bimetallic nanoparticles: Insights from a phase-field model, Acta Materialia **233**, 117933 (2022).
[16] D. A. Cogswell and W. C. Carter, Thermodynamic phase-field model for microstructure with multiple components and phases: The possibility of metastable phases, Physical Review E **83**, 061602 (2011).
[17] D. A. Cogswell, *A phase-field study of ternary multiphase microstructures*, Ph.D. thesis, Massachusetts Institute of Technology (2010).
[18] J. Zhu, L.-Q. Chen, J. Shen, and V. Tikare, Coarsening kinetics from a variable-mobility Cahn-Hilliard equation: Application of a semi-implicit Fourier spectral method, Physical Review E **60**, 3564 (1999).
[19] H. Cook, Brownian motion in spinodal decomposition, Acta Metallurgica **18**, 297 (1970).
[20] L. Li, X. Li, Z. Duan, R. J. Meyer, R. Carr, S. Raman, L. Koziol, and G. Henkelman, Adaptive Kinetic Monte Carlo simulations of surface segregation in PdAu nanoparticles, Nanoscale **11**, 10524 (2019).
[21] P. Grammatikopoulos, J. Kioseoglou, A. Galea, J. Vernieres, M. Benelmekki, R. E. Diaz, and M. Sowwan, Kinetic trapping through coalescence and the formation of patterned Ag–Cu nanoparticles, Nanoscale **8**, 9780 (2016).
[22] F. Haider, R. Kozubski, and T. Abinandanan, Simulation techniques, in *Alloy Physics* (John Wiley & Sons, Ltd, 2007) Chap. 12, pp. 653–706.
[23] A. Dinsdale, SGTE data for pure elements, Calphad **15**, 317 (1991).
[24] P. Subramanian and J. Perepezko, The Ag-Cu (silver-copper) system, Journal of Phase Equilibria **14**, 62 (1993).
[25] T. Tanaka and S. Hara, Thermodynamic evolution of nanoparticle binary alloy phase diagrams, Zeitschrift fuer Metallkunde/Materials Research and Advanced Techniques **92**, 1236 (2001).
[26] K. D. Malviya and K. Chattopadhyay, Synthesis and mechanism of composition and size dependent morphology selection in nanoparticles of Ag–Cu alloys processed by laser ablation under liquid medium, The Journal of Physical Chemistry C **118**, 13228 (2014).
[27] C.P. Wang, L.N. Yan, J.J. Han, and X.J. Liu, Diffusion mobilities in the fcc Ag–Cu and Ag–Pd alloys, Calphad **37**, 57 (2012).
[28] J. W. Cahn, On spinodal decomposition, Acta Metallurgica **9**, 795 (1961).
[29] J. W. Cahn, Critical point wetting, The Journal of Chemical Physics **66**, 3667 (1977).

APPENDIX: NON-DIMENSIONALIZATION PROCEDURE

We make the governing equations (Eqs. (1) and (3)) dimensionless by using dividing the length, energy and time variables by their characteristic values (L_c, E_c, and τ_c, respectively):

$$x = x'/L_c, f = f'/E_c, t = t'/\tau_c, \tag{14}$$

where the primed quantities represent the dimensional values of the variables. Now we write the dimensional form of Eq. (1) and use the above relations to make it non-dimensional (noting that the dimensional gradient operator ∇' has the dimension of inverse of length):

$$\begin{aligned}
\mathscr{F}' &= \frac{1}{V_m'}\int_\Gamma \left[f'(c,\phi) + \kappa_\phi' |\nabla'\phi|^2 + \kappa_c' |\nabla c|^2\right] d\Gamma' \\
\Rightarrow E_c\mathscr{F} &= \frac{1}{L_c^3 V_m}\int_\Gamma \Big[E_c f(c,\phi) + (1/L_c^2)\kappa_\phi' |\nabla\phi|^2 \\
&\quad + (1/L_c^2)\kappa_c' |\nabla c|^2\Big] L_c^3 d\Gamma, \\
\Rightarrow \mathscr{F} &= \frac{1}{V_m}\int_\Gamma \left[f(c,\phi) + \frac{\kappa_\phi'}{E_c L_c^2}|\nabla\phi|^2 + \frac{\kappa_c'}{E_c L_c^2}|\nabla c|^2\right] d\Gamma
\end{aligned} \tag{15}$$

Thus we see that we get back the original form of Eq. (1) in terms of non- dimensional variables when κ_c' and κ_ϕ' are scaled by choosing a reference value of $\kappa = E_c L_c^2$.

The Cahn-Hilliard equation (Eq. 3) in dimensional form is converted to its non-dimensional form as follows:

$$\begin{aligned}
\frac{\partial c}{\partial t'} &= \nabla' \cdot M' \nabla' \Big(\frac{\delta \mathscr{F}'}{\delta c} \Big) \\
\Rightarrow \frac{1}{\tau_c} \frac{\partial c}{\partial t} &= \frac{1}{L_c} \nabla \cdot \frac{1}{L_c} M' \nabla \Big[\frac{\delta (E_c \mathscr{F})}{\delta c} \Big] \\
\Rightarrow \frac{\partial c}{\partial t} &= \nabla \cdot \frac{E_c \tau_c}{L_c^2} M' \nabla \Big(\frac{\delta \mathscr{F}}{\delta c} \Big) \qquad (16)
\end{aligned}$$

Thus we get back the non-dimensional Eq. (3) by scaling the dimensional mobility M' with its characteristic value $L_c^2/E_c\tau_c$. Using these conversion expressions and choosing appropriate values for the reference variables L_c, E_c and τ_c, the dimensionless model parameters used in the simulations can now be connected to their dimensional counterparts [15].

Choosing $L_c = (V_m/N_0)^{1/3}$ where N_0 is the Avogadro's number gives a reference length of ~ 0.25 nm. If reference energy is taken as $k_B T_c$, it yields a value of $E_c = 1.863 \times 10^{-20}$ J $= 0.116$ eV for $T_c = 1350$ K. Finally, a reference time can be obtained, for example, by using a typical mobility value [27] of $M' \approx \dfrac{1.8 \times 10^{-18}}{k_B T}$ m^2/Js, which for $T = 800$ K yields $\tau_c = L_c^2/E_c M' \approx 21$ ms. Dimensional values of relevant model parameters, along with their conversion factors, are listed in Table II, while the corresponding values of surface and interfacial energies resulting from different parameter sets are provided in Table III.

TABLE II: Simulation parameters (all energies are in *per atom* basis). Conversion factors from non-dimensional to dimensional form are based on characteristic length $L_c = 0.25\,\text{nm}$, characteristic energy $E_c = 0.116\,\text{eV}$ and characteristic time $\tau_c = 21\,\text{ms}$.

Parameter name	Symbol	Value		Conversion factor
		Non-dimensional	Dimensional	
Grid size	Δx	0.5	0.125 nm	L_c
Time step	Δt	0.001	21 µs	L_c^2/E_cM'
Particle diameter	d	140	35 nm	L_c
Matrix free energy coefficient	f_0^m	2	0.232 eV	E_c
Particle free energy coefficient	f_0^p	2, 4, 6, 8	0.23, 0.46, 0.69, 0.93 eV	E_c
Barrier height	ω_0	3.75, 5, 6, 12	0.43, 0.58, 0.67, 1.39 eV	E_c
Gradient energy coefficient	κ_c	1, 2, 8	0.007, 0.014, 0.06 eVnm^2	$E_cL_c^2$
	κ_ϕ	1	0.007 eVnm^2	$E_cL_c^2$

TABLE III: Non-dimensional (first sub-row in a row) and dimensional (second sub-row in a row) values of surface and interfacial energies. Unit for the dimensional values is mJm^{-2}.

$(f_0^p,\ \kappa_c,\ \omega_0)$	σ_1	σ_2	σ_{12}
$(8, 1, 12)$	4.19	3.09	0.94
	1248	921	280
$(6, 2, 3.75)$	1.77	1.44	1.15
	527	429	343
$(4, 1, 6)$	2.21	1.76	0.67
	658	524	200
$(2, 8, 6)$	2.24	1.86	1.33
	667	554	396
$(4, 2, 5)$	1.98	1.6	0.94
	590	477	280